Application of flat plate latent heat thermal energy storage for waste heat recovery and energy flexibility in maritime sector

Lorenzo Ciappi[a], Pouriya Niknam[b], Robin Fisher[c] and Adriano Sciacovelli[d]

[a] *University of Birmingham, Birmingham, UK, l.ciappi@bham.ac.uk*
[b] *University of Birmingham, Birmingham, UK, p.niknam@bham.ac.uk,*
[c] *University of Birmingham, Birmingham, UK, r.fischer@bham.ac.uk*
[d] *University of Birmingham, Birmingham, UK, a.sciacovelli@bham.ac.uk, CA*

Abstract:

Thermal energy storage (TES) fosters the use of renewable energy, improves the efficiency of existing processes and enhances the flexibility of energy availability. Extensively researched and applied in buildings, TES is still in the early stages of its evolution regarding other relevant applications for which decarbonisation of heat exchange is paramount. This is the case in the maritime sector. Therefore, this research proposes a novel modular latent heat thermal energy storage (LHTES) system functioning with a phase change material (PCM) as an energy storage medium for installation on ships. An analytical model was developed relying on a theoretical approach consolidated in the literature. Firstly, the model was validated through the comparison with a reference case. Then, it was utilised for evaluating the functioning of various configurations of a TES device operating on board a vessel. The performance of the proposed system was investigated during the charging and discharging phases considering operating conditions typical of cruising and cargo vessels. The effects of device length and height were assessed and the influence of these parameters on the amount of energy stored and energy storage density was determined. Overall, the paper provides an innovative application of TES technology and highlights the wider benefits of energy storage in the maritime sector.

Keywords:

Thermal energy storage; latent heat; maritime decarbonisation; waste heat recovery; PCM.

1. Introduction

The functioning of the vast majority of energy systems is currently based on transforming the energy of fuel into useful work for their scopes and waste heat released to the environment. This energy inefficiency is a paramount problem mainly for industrial thermal processes, heating systems and transportation. Heat wastage significantly affects marine applications, especially cruising and cargo vessels. Two-stroke internal combustion diesel engines represent the propulsion system of around 96% of modern civilian ships above 100 t of mass [1]. These engines have values of efficiency lower than 50% with the consequent wastage of at least half of fuel energy through cooling fluid streams and exhaust gases [2]. The thermal energy released is responsible for about 3% of total greenhouse gas emissions (GHG) worldwide and this level is expected to rise together with the global trade through shipping [3]. Since 2011, the International Maritime Organisation (IMO) is applying regulations for controlling air and water pollution with the aim of halving emissions by 2050 [4].

The reduction of GHG emissions can be successfully achieved by enhancing energy efficiency. Improvements to the existing engines and the use of other technologies on board were widely proposed for this purpose [5]. It is estimated that total engine efficiency could be boosted from 50% to 60% and fuel efficiency could be raised from 4% to 16% [1,2]. Regarding the energy source, alternative fuels to the traditional high sulphur fuel such as liquefied natural gas (LNG), hydrogen, ammonia and advanced bio-fuels can be utilised and auxiliary propulsion devices such as modern sails and renewable systems such as solar photovoltaic panels and solar hybrid devices can be placed on board. Concerning the direct limitation of carbon emissions, carbon capture and storage systems can be installed. Integrating these technologies with waste heat recovery (WHR) devices would foster the enhancement of vessel efficiency as at least half of fuel energy is lost by way of heat. Currently, the WHR systems used on vessels are waste heat boilers, steam turbine cycles or turbocharging devices. However, more sophisticated WHR solutions could be effectively installed on board for harnessing thermal energy from exhaust flue gases of diesel engines and their cooling fluids such as jacket water and lubricants.

The main technologies exploiting heat wastage are thermal energy storage (TES) systems, organic Rankine cycles, sorption desalination and refrigeration devices and isobaric expansion engines. They transform the thermal power losses of the engine into mechanical or electrical power (waste heat-to-power), cooling power (waste heat-to-cold), or they upgrade the excess thermal energy to generate added value for on-board demands such as steam or desalinated water.

The presented research regards the development of an analytical model for solving heat transfer in a TES device constituted by a flat plate heat exchanger functioning with air or water as a heat exchange fluid (HTF) and a phase change material (PCM) as an energy storage medium. The Methodology section defines the theoretical model developed and the finite element approximation strategy applied. The Results and discussion section first describes the process of the validation of the model through the comparison with consolidated literature data. Then, it shows the application of the model for evaluating the performance of five configurations of a TES device for the possible installation on board a vessel. Operating conditions typical of cruising and cargo vessels were considered.

2. Methodology

A theoretical model of a latent heat thermal energy storage (LHTES) system was developed for evaluating the behaviour of heat exchangers with multi-layer rectangular plates functioning with a heat transfer fluid to warm or cool a phase change material.

2.1. Modelling equations

The model of the multi-layer rectangular LHTES system relies on consolidated theoretical approaches present in the literature [6,7] and was successfully used for technical applications [8–10]. The methodology is based on three hypotheses regarding the heat transfer transformations.

- The axial conduction in the fluid is negligible during flow.
- The temperature gradients normal to the flow are negligible due to the sufficiently low Biot number.
- The heat losses outside of the domain are negligible.

The schematic of the model developed is illustrated in Figure 1. The heat transfer fluid with mass flow rate $\dot{m}_f$ and inlet temperature $T_{f,inl}$ crosses the device along the axial direction x passing through the cavities delimited by flat plates with PCM. The fluid can be a gas or a liquid. The phase change material is positioned between the flat plates of length L, total cross-sectional area A, and wetted perimeter P.
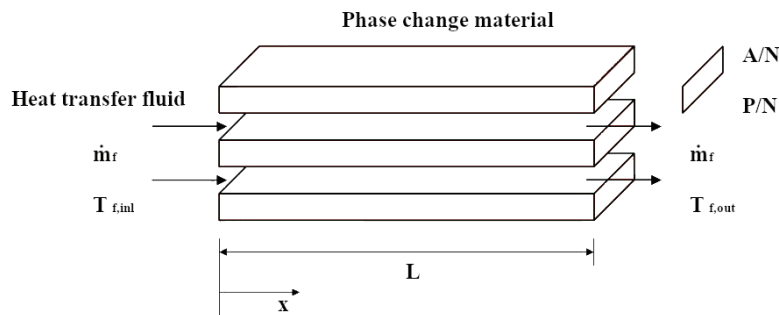

Figure 1. Scheme of a TES device with flat plate containers.

The set of equations imposing energy balance for the phase change material and the heat transfer fluid are stated in Eq. (1).

$$\begin{cases} \dfrac{\partial u}{\partial t} = \dfrac{k}{\rho}\dfrac{\partial^2 T}{\partial x^2} + \dfrac{UP}{\rho A}\left(T_f - T\right) \\ \dfrac{\partial T_f}{\partial t} = -\dfrac{\dot{m}_f}{\rho_f A_f}\dfrac{\partial T_f}{\partial x} + \dfrac{UP}{\rho_f A_f cp_f}\left(T - T_f\right) \end{cases} \tag{1}$$

where u, T, ρ and k are the specific internal energy, temperature, density, and thermal conductivity of PCM, T_f, ρ_f, c_{pf} and A_f are the temperature, density, specific heat and flow area of HTF, t is time and U is the overall heat transfer coefficient between the two materials.

The specific internal energy u depends on the temperatures of the HTF and PCM and the thermo-physical properties of the PCM based on Eq. (2).

$$\begin{cases} c_s(T - T_{ref}) & if\ T < T_m \\ c_s(T_m - T_{ref}) + \chi F & if\ T = T_m \\ c_s(T_m - T_{ref}) + F + c_l(T - T_m) & if\ T > T_m \end{cases} \tag{2}$$

where c_l and c_s are the values of the specific heat of the liquid and solid phases of the PCM, χ is its liquid mass fraction, T_m is its melting temperature, F is its latent heat of fusion and T_{ref} is the reference temperature corresponding to the null internal energy.

The general formulation of the energy balance of Eq. (1) can be simplified considering that the heat transfer due to axial conduction in the PCM during flow is negligible and assuming a low capacitance for the HTF. In these circumstances, the energy balance reduces to Eq. (3).

$$\begin{cases} \dfrac{\partial u}{\partial t} = \dfrac{UP}{\rho A}(T_f - T) \\ \dfrac{\partial T_f}{\partial x} = \dfrac{UP}{\dot{m}_f c p_f}(T - T_f) \end{cases} \tag{3}$$

The governing equations can be reformulated in a non-dimensional form in terms of the number of transfer units NTU as in Eq. (4) through the normalisation relying on the temperature difference between the PCM melting temperature and the reference temperature [6].

$$\begin{cases} \dfrac{\partial \bar{u}}{\partial \tau} = (\theta_f - \theta) \\ \dfrac{\partial \theta_f}{\partial \zeta} = NTU(\theta - \theta_f) \end{cases} \tag{4}$$

The normalisation procedure is based on the non-dimensional distance ζ defined as the ratio between the axial position x and plate length L and the equations from Eq. (5) to Eq. (9) that provide the non-dimensional temperature differences of the PCM and HTF θ and θ_f, the non-dimensional heat transfer coefficient $\bar{u}$ and the time τ.

$$\theta = \frac{T - T_{ref}}{T_m - T_{ref}} \tag{5}$$

$$\theta_f = \frac{T_f - T_{ref}}{T_m - T_{ref}} \tag{6}$$

$$\bar{u} = \frac{u}{c(T_m - T_{ref})} \tag{7}$$

$$\tau = \frac{tUPL}{\rho ALc} \tag{8}$$

$$NTU = \frac{UPL}{\dot{m}_f c_{pf}} \tag{9}$$

2.2. Finite difference approximation

The solution of the differential governing equations defined in the NTU formulation was achieved through the finite differencing technique [6]. This approach is based on the subdivision of the storage system into a set of n axial nodes as illustrated in Figure 2.
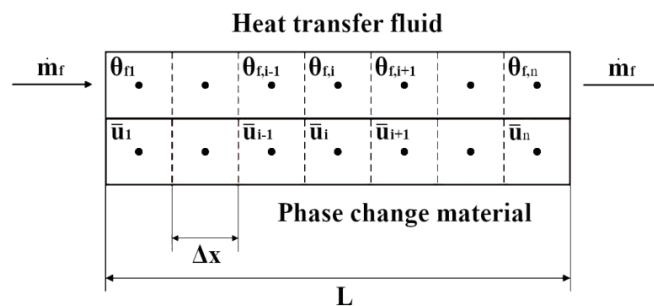

Figure 2. Scheme of the computational domain composed by a set of nodes.

At the beginning of each time step, the PCM internal energy, the HTF temperature at the axial nodes and the current inlet fluid temperature are known. Forward differencing techniques are then applied for updating these quantities. Therefore, the energy balance is expressed for each nodal position i from 1 to n through Eq. (10).

$$\begin{cases} \bar{u}'_i = \bar{u}_i + \Delta\tau\left(\theta_{f,i} - \theta_i\right) \\ \theta'_{f,i+1} = \theta'_{f,i} + \Delta\zeta NTU\left(\theta_i - \theta_{f,i}\right) \end{cases} \tag{10}$$

where the superscript refers to the variable at the new time step, $\Delta\tau$ is the non-dimensional time step and $\Delta\zeta$ is the non-dimensional nodal spacing.

The first formula of the set of Eq. (10) states that the change in PCM internal energy during the time step equals the heat transferred from the HTF to the PCM within this period. In analogy, the second equation indicates that the variation in HTF enthalpy from one node to the adjacent one equals the heat added by convection.

At each time step and for every node, Eq. (10) is applied for computing the non-dimensional values of the PCM internal energy $\bar{u}'_i$ and the HTF temperature at the end of the time step based on the known values of $\bar{u}_i$, θ_i and $\theta_{f,i}$ and the updated inlet flow temperature $\theta'_{f,i}$. At first, the updated HTF temperatures are determined and then the PCM internal energy of every corresponding node is defined.

The temperature and quality of all the PCM nodes are updated with Eq. (11) based on the liquid mass fraction provided by Eq. (12). The assumption of equivalent values of the specific heat of the liquid and solid phases of PCM is imposed.

$$\bar{u} = \theta + \frac{F}{c\left(T_m - T_{ref}\right)}\chi \tag{11}$$

$$\begin{cases} \chi = 0 & if\ \theta < 1 \\ 0 \le \chi \le 1 & if\ \theta = 1 \\ \chi = 1 & if\ \theta > 1 \end{cases} \tag{12}$$

The finite difference solution tends to the exact one by increasing the node number as a procedure for the discretisation of the computational domain is applied. It was shown in the literature that five nodes are sufficient for representing the TES device with a good approximation [6].

3. Results and discussion

The analytical model was validated through the comparison with a reference case selected in the literature regarding multi-layer thermal energy storage systems with PCM. Afterwards, the model was applied for evaluating the functioning of a TES device operating on board a vessel.

3.1. Model validation

A literature reference case was selected to validate the analytical model developed for assessing the process of heat transfer in TES devices operating with a phase change storage medium composed of cavities with parallel flow paths [9]. The schematic of the thermal energy system of the reference literature case is coherent with that of Figure 1 and its main geometric specifications are indicated in Table 1.

Table 1. Geometric parameters of the heat exchanger defined in the reference case [9].

Parameter	Symbol	Value	Unit
PCM layer number	N	3	-
Fluid channel number	N_f	2	-
PCM layer thickness	b	0.005	m
Fluid channel thickness	b_f	0.003	m

The complete definition of the model geometry requires the assumption of the dimensional value of the plate length and width. In the analyses conducted, equal dimensional values of 0.03, 0.04 and 0.05 m were imposed for these parameters. The wetted perimeter and cross-sectional area of the PCM layers were computed based on their width and thickness. The geometric parameters used in the calculations in addition to those defined in the reference case are defined in Table 2.

Table 2. Geometric parameters of the PCM layers assigned in the analyses.

Parameter	Symbol	Value	Unit
Plate length	L	0.03–0.05	m

Plate width	W	0.03–0.05	m
PCM perimeter	P	0.21–0.33	m
PCM area	A	4.50–7.50	cm^2

The heat transfer fluid crossing the cavities of the device is air and the storage medium is Glauber's salt (sodium sulphate decahydrate).

The physical properties and initial conditions of the PCM defined in the literature reference are listed in Table 3. In the reference case, the liquid state specific heat of the Glauber's salt is 3.26 kJ/kg/K. However, in the simplified model developed the specific heat of the liquid state is assumed equivalent to the value of the solid state, which is equal to 1.92 kJ/kg/K. The reference temperature for the simulations was set to 20°C.

Table 3. Physical properties and initial conditions of the Glauber's salt [9].

Parameter	Symbol	Value	Unit
Inlet temperature	T_{inl}	25	°C
Melting temperature	T_m	32	°C
Solid state density	ρ_s	1460	kg/m^3
Liquid state density	ρ_l	1330	kg/m^3
Solid state specific heat	c_s	1.92	kJ/kg/K
Specific latent heat of fusion	F	251	kJ/kg
Solid state thermal conductivity	k_s	0.514	W/m/K
Liquid state thermal conductivity	k_l	0.514	W/m/K

The temperature of the air at the domain inlet is 90°C and the initial temperature of the Glauber's salt is 25°C. Thus, the thermo-physical properties of air were evaluated at the average temperature of 57.5°C and the atmospheric pressure.

The characteristic length l of the flow cavities was calculated with Eq. (13). This parameter and the Nusselt number N_u of 8.235 defined in the reference case were utilised to determine the overall heat transfer coefficient U between the HTF and PCM through Eq. (14).

$$l = \frac{4A_f}{P_f} \tag{13}$$

$$U = \frac{N_u k_f}{l} \tag{14}$$

where P_f and A_f are the perimeter and area of the fluid channels regarding the PCM layer number and k_f is the air thermal conductivity.

The air velocity v_f was computed with Eq. (15) based on the Nusselt number, the Prandtl number P_r, the Reynolds number R_e, the dynamic viscosity μ and the density of the airflow and the characteristic length of the flow cavities.

$$v_f = \left(\frac{N_u}{0.664 P_r^{1/3}}\right)^2 \frac{\mu_f}{\rho_f l} \tag{15}$$

The time corresponding to the non-dimensional time t^* of 14 of the literature case was determined with Eq. (16) for comparing the results of the two models [9].

$$t = t^* \frac{\rho_s c_s b^2}{4 k_s} \tag{16}$$

The values of the above parameters applied in the simulations are resumed in Table 4.

Table 4. Parameters and operating conditions used in the simulations of the reference case [9].

Parameter	Symbol	Value	Unit
Characteristic length	l	0.00545–0.00566	m
Nusselt number	N_u	8.235	-
Overall heat transfer coefficient	U	0.0426–0.0411	kW/m^2/K
Average air velocity	v_f	0.66–0.64	m/s
Air mass flow rate	$\dot{m}_f$	0.00013–0.00020	kg/s
Reference non-dimensional time	t^*	14	-

Reference time	t	477.2	s

The validation of the theoretical model was achieved through the comparison with the literature reference [9]. The results of the two models were confronted by analysing the predicted time series of the liquid mass fraction and temperature of the HTF and PCM. In Figure 3(a), the increase of the mass fraction of the liquid phase of the PCM is presented as a function of time. The convective heat transfer coefficient decreases as the plate size increases. The lower rate of heat exchange with growing dimensions determines a rise in the time required for reaching equilibrium. In the reference case, the complete melting of the PCM is obtained at time 477.2 s when the average liquid mass fraction equals the unit and the device is fully charged. For the simulation performed, the melting time is 1102, 1411 and 1710 s based on the increasing plate dimensions. The curves have a similar trend, indicating that the simplified analytical model proposed is capable of evaluating the melting process.

Figure 3(b) illustrates the liquid mass fraction computed at each domain node for the device with a length and a width equal to 0.04 m. The amount of time required for melting rises from the first to the last node due to the reduction of the temperature of the HTF across the flow cavities for the progressive reduction of the heat transfer rate.
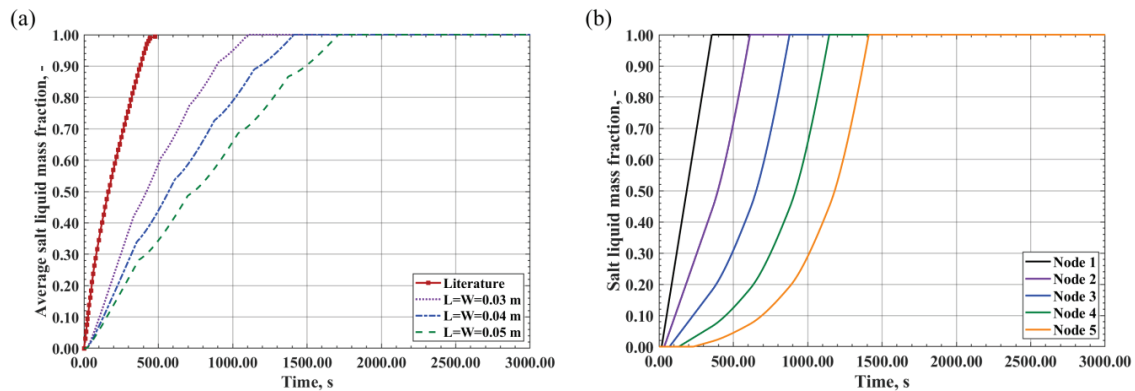

Figure 3. Time series of the liquid fraction of the Glauber's salt: (a) average values for the reference case and different plate dimensions, (b) values at the nodes for the device with the intermediate plate size.

Figure 4(a) depicts the increase in the average temperature of the Glauber's salt for the three configurations analysed. The rate of rise is greater reducing plate size for the higher heat transfer owing to the lower mass airflow rate. The average temperature of the PCM is 54.6°C corresponding to the instant of complete melting for the literature case. For the three configurations analysed, the values obtained for this parameter are 73.53, 75.43 and 76.58°C, respectively. The higher predictions are attributable to the specific heat of the liquid phase of the PCM that is assumed equivalent to that of the solid phase in the simplified model proposed.

In Figure 4(b), the temperature of Glauber's salt calculated at the five nodes is presented as a function of time during the charging process. The time required for heating up the PCM to the temperature of the HTF rises increasing the distance from the domain inlet as the rate of heat transfer decreases along the channel length.
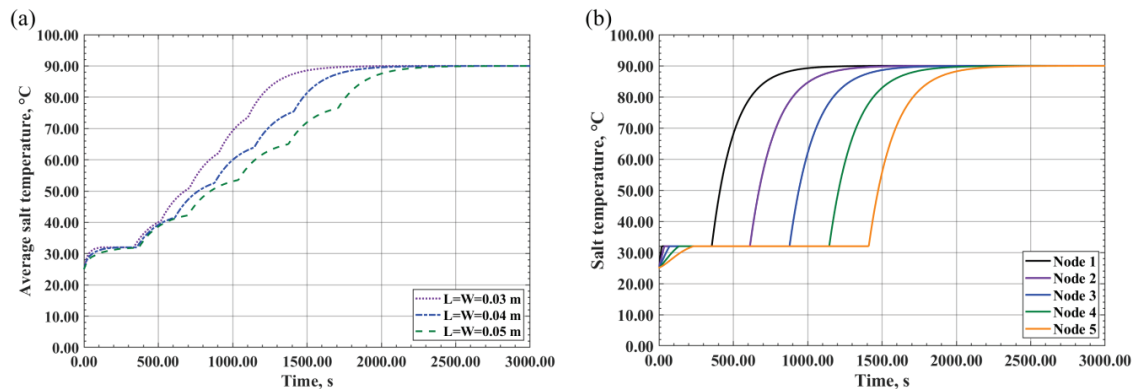
Figure 4. Time series of the temperature of the Glauber's salt: (a) average values for the reference case and different plate dimensions, (b) values at the nodes for the device with the intermediate plate size.

In Figure 5(a), the air temperature at the outlet of the TES device is shown as a function of time for the three configurations analysed. The temperature of the HTF increases with time as the PCM melts. When the PCM is completely melted, the temperature values are 60.55, 55.47 and 49.91°C, respectively. The temperature of the airflow exiting the device approaches the initial temperature of the PCM. The temperature difference reduces by increasing the plate size due to the enhancement of heat transfer.

Figure 5(b) presents the air temperature calculated at the five nodes of the computational domain. In particular, the temperature of node 1 is constant and equals the inlet temperature of 90°C of the charging fluid. The values of the other nodes rise up to 90°C requiring higher time as the distance from the domain inlet grows. The curves of the last three nodes indicate the presence of instabilities at the end of the melting transformation which could be minimised by increasing the number of axial nodes and reducing the time step size.
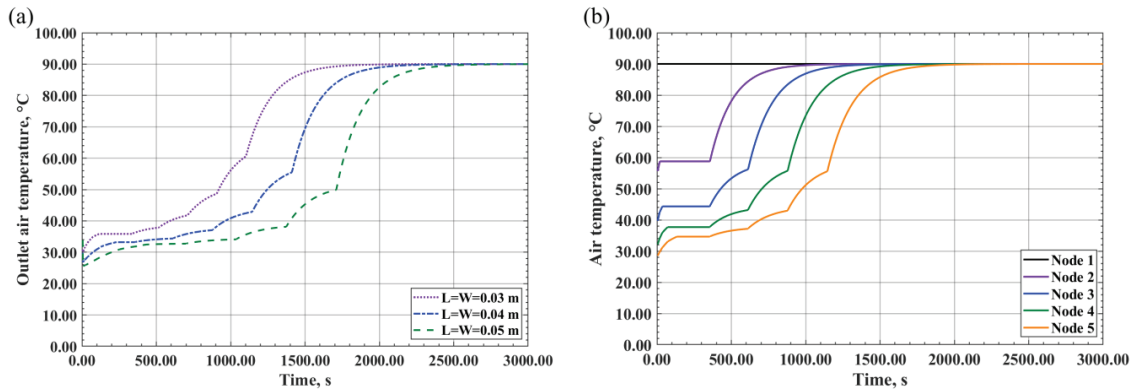

Figure 5. Time series of the air temperature: (a) values at the outlet for the reference case and different plate dimensions, (b) values at the nodes for the device with the intermediate plate size.

3.2. Case study

The TES device considered for the possible application on a vessel is a flat plate heat exchanger similar to the schematic illustrated in Figure 6. The plates are stacked parallel to each other and are bundled in a box where they are submerged in the phase change material. At each upper extremity of the device, a plenum manifold connects the pipe of the heat transfer fluid with all the plates.
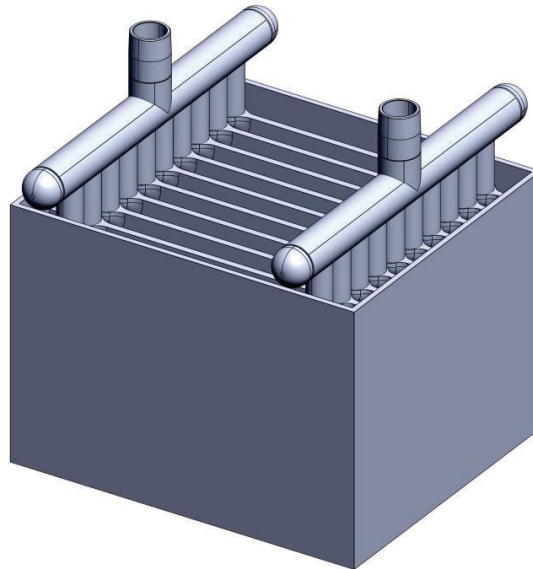

Figure 6. Schematic of the structure of the heat exchanger with the box, plates and pipes.

Five configurations of the TES devices for vessel application were investigated for evaluating the effects of plate dimensions on performance. A set of 10 plates with fixed values of thickness of the PCM layers and fluid channels was considered. The length and height of the device were varied to explore sizes comparable with traditional heat exchangers with submerged flat plates [11]. The length was assigned in the range from 0.8 to 1.2 m with intervals of 0.1 m and the height was set at 80% of the length. The geometric parameters defining the configuration of the case study are listed in Table 5.

Table 5. Geometric parameters of the TES device configurations considered for operating on a vessel.

Parameter	Symbol	Value	Unit
Plate length	L	0.80–1.20	m
Plate height	H	0.64–0.96	m
PCM layer thickness	b	0.030	m
Fluid channel thickness	b_f	0.018	m
PCM layer number	N	11	-
Fluid channel number	N_f	10	-
PCM perimeter	P	14.74–21.78	m
PCM area	A	0.2112–0.3168	m^2

The system uses water as heat transfer fluid and H105 as phase change material. This is an inorganic salt with the chemical formulation KNO_3 which is in the form of granules. This storage medium was selected as its melting temperature has a value close to the average of the charging and discharging temperatures of the water [12].

The physical properties and initial conditions of the PCM are provided in Table 6. The hypothesis of equal values of the specific heat of the solid and liquid phases was applied. The reference temperature of 20°C was considered in the calculations.

Table 6. Physical properties and initial conditions of the H105 [12].

Parameter	Symbol	Value	Unit
Inlet temperature	T_{inl}	90	°C
Melting temperature	T_m	104	°C
Solid state density	ρ_s	1700	kg/m^3
Solid state specific heat	c_s	1.50	kJ/kg/K
Specific latent heat of fusion	F	125	kJ/kg
Solid state thermal conductivity	k_s	0.500	W/m/K
Liquid state thermal conductivity	k_l	0.500	W/m/K

The water charges the device at 120°C and discharges it at 90°C in compliance with typical scenarios of heat wastage on vessels. A total mass flow rate of 1.50 kg/s was selected, resulting in a mass flow rate of 0.15 kg/s for each plate. The thermo-physical conditions of the water charging the device were evaluated at the average temperature of 105°C and the pressure of 3 atm.

The formulation of Eq. (13) was applied to determine the characteristic length *l* of the device. Since the mass flow rate of the device was imposed, the average velocity of the water flowing through the cavities was determined relying on the water density and the cross-sectional area of the cavity. Thus, the Nusselt number was calculated with Eq. (15) and then the overall heat transfer coefficient between the HTF and PCM was computed with Eq. (14). The parameters applied in the simulations and the duration of the analyses are listed in Table 7.

Table 7. Parameters and operating conditions used in the simulations of the case study.

Parameter	Symbol	Value	Unit
Water mass flow rate	$\dot{m}_f$	1.50	kg/s
Average water velocity	v_f	0.0136–0.0091	m/s
Characteristic length	l	0.03502–0.03534	m
Overall heat transfer coefficient	U	0.6298–0.5119	$kW/m^2/K$
Nusselt number	N_u	32.48–26.64	-
Time	t	6000	s

In Figure 7(a), the process of the phase change of the H105 is shown in terms of variation in time of the liquid mass fraction. Increasing the dimensions of the plates, the convective heat transfer coefficient reduces extending the time required for the charge. The duration of the melting process is 701, 819, 946, 1082 and 1226 s as the size increases. In analogy, the time for the solidification process is 797, 929, 1072, 1225 and 1386 s. Therefore, the charging phase is faster than the discharging phase. This is caused by the different contributions of heat transfer for conduction and natural convection in the melting and solidification processes.

Figure 7(b) indicates the variation in time of air temperature along the plate length at each domain node. The device with an intermediate size with a length of 1 m and a height of 0.8 m was considered for presenting the results. The time of melting and solidification increases from the first to the last node as the water temperature decreases flowing through the cavities. This determines a progressive reduction of heat transfer along plate length.
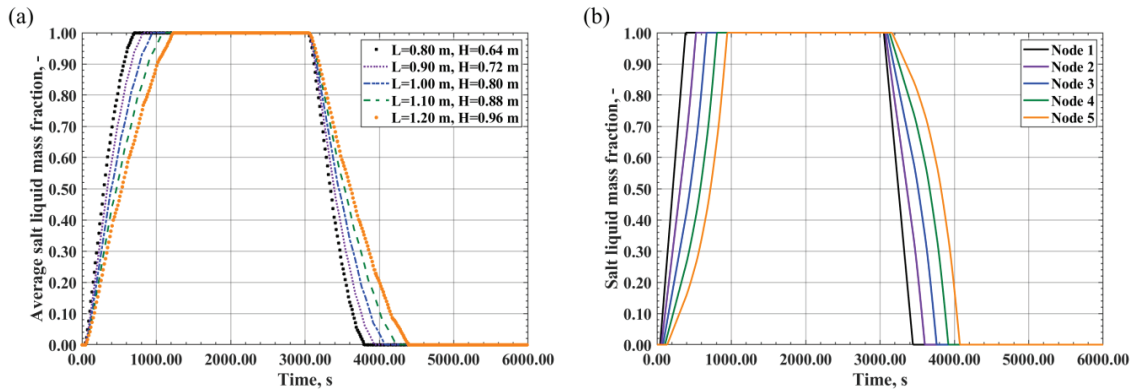
(a)

(b)

Figure 7. Time series of the liquid fraction of the H105 salt: (a) average values for the configurations investigated, (b) values at the domain nodes for the device with the intermediate size.

In Figure 8(a), the variation in the average temperature of the H105 salt during charging and discharging is depicted. The temperature gradients of both phase transformations are higher for the nodes close to the domain inlet for the reduction of the heat transfer in the direction of plate length. The discontinuities in the rate of rise of the temperature gradients of the salt are attributable to the presence of the interface between solid and liquid and to the duration of phase change along plate length, which is visible in Figure 8(b). The temperature gradients are higher during melting than solidification in accordance with the different duration of the two transformations. The average values of the temperature of the PCM at complete melting are equal to 115.90, 116.16, 116.35, 116.49 and 116.57°C for the various configurations. At complete solidification, the average temperatures correspond to 93.39, 93.25, 93.09, 92.97 and 92.95°C.
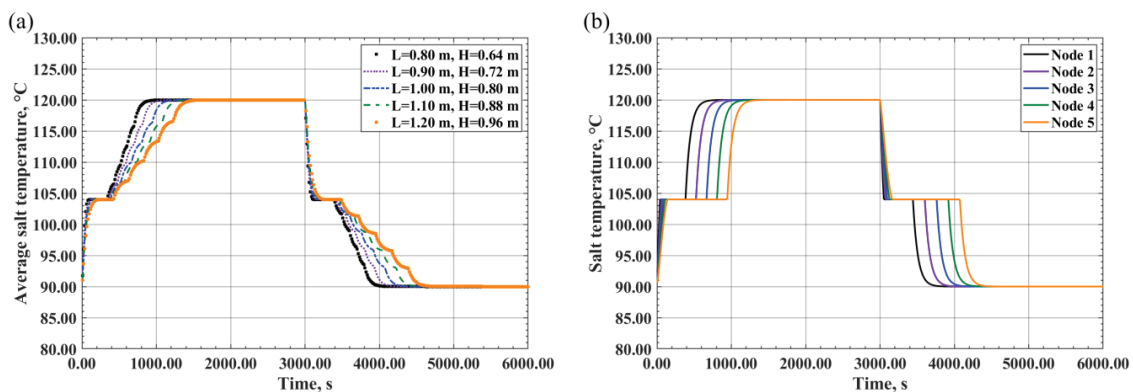
(a)

(b)

Figure 8. Time series of the temperature of the H105 salt: (a) average values for the configurations investigated, (b) values at the domain nodes for the device with the intermediate size.

The time series of the water temperature at the domain outlet is illustrated in Figure 9(a) for the five TES configurations. The HTF temperature rises during charging and decreases during discharging. The rate of rise is higher in the former process and it increases by reducing plate size due to the greater heat transfer.

The outlet water temperature in the charging phase is 115.45, 114.91, 114.31, 113.66 and 112.95°C based on the increasing device size, while it is 93.83, 94.33, 94.87, 95.45 and 96.09°C in the discharging phase. Figure 9(b) shows the water temperature computed at the five nodes along the domain. The temperature of the first node equals the values of the charging and discharging fluid during the relative phases. For the other nodes, the rate of variation increases moving from the inlet to the outlet.
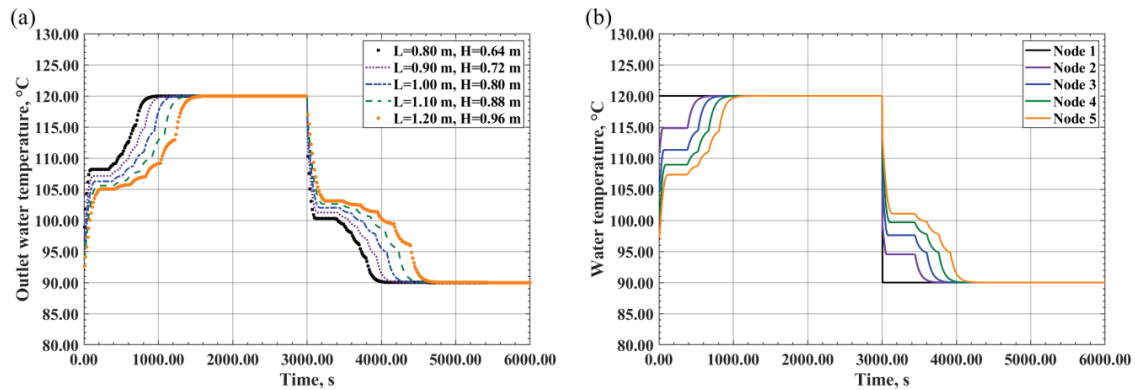

Figure 9. Time series of the water temperature: (a) values at the outlet for the configurations investigated, (b) values at the domain nodes for the device with the intermediate size.

The performance of the TES devices was evaluated in terms of volume and mass of the TES device, energy storage of the PCM and energy storage density, defined by the ratio between the first two parameters. The data achieved for the five configurations investigated are listed in Table 8. The selection of the best-suited configuration for the vessel application depends on the availability of thermal energy and the space and weight constraints on board vessels. The energy storage density slightly increases with device dimensions for the design space explored.

Table 8. Performance parameters of the TES devices analysed for the vessel application.

Parameter	Case 1	Case 2	Case 3	Case 4	Case 5	Unit
Volume	0.30	0.37	0.46	0.55	0.66	m^3
Mass	474	594	727	874	1034	kg
Energy storage	13.56	17.17	21.19	25.64	30.52	kWh
Energy storage density	45.57	45.85	46.07	46.26	46.41	kWh/m^3

4. Conclusions

A novel modular latent heat thermal energy storage (LHTES) system was proposed for the installation on cruising and cargo vessels. The main aim of the research is to increase the energy efficiency of ships for reducing the carbon emissions of the maritime sector. Moreover, these devices allow stabilising energy availability on board by smoothing the intermittency of thermal energy wastage. A theoretical methodology consolidated in the literature was applied to develop a fast and reliable analytical model capable of investigating a wide variety of geometric configurations and operating conditions. The code solves the heat exchange between the heat transfer fluid (HTF) and the phase change material (PCM) during the charging and discharging phases. It was found that the discharging time is longer than the charging time, which stems from the different contributions of conduction and natural convection heat transfer in melting and solidification. Operating conditions characteristic of cruising and cargo vessels were considered for evaluating the performance of a set of thermal energy storage (TES) device configurations. Geometric parameters suitable for their on-board application were selected to analyse a proper design space. The effects on the main performance indicators were assessed by varying the plate length between 0.80 and 1.20 m and the plate height from 0.64 to 0.96 m while keeping fixed the number of plates and the thickness of the HTF channels and PCM layers. The energy stored is between 13.56 and 30.52 kWh and the energy storage density ranges from 45.57 to 46.41 kWh/m^3.

Nomenclature

Roman symbols

A area, m^2

b thickness, m

Greek symbols

ζ non-dimensional distance, -

θ non-dimensional temperature difference, -

c	specific heat, J/kg/K		μ	dynamic viscosity, Pa·s
cp	constant pressure specific heat, J/kg/K		ρ	density, kg/m^3
F	specific latent heat of fusion, kJ/kg		τ	non-dimensional time, -
H	height, m		χ	liquid mass fraction, -

c   specific heat, J/kg/K

cp   constant pressure specific heat, J/kg/K

F   specific latent heat of fusion, kJ/kg

H   height, m

k   thermal conductivity, W/m/K

L   length, m

l   characteristic length, m

$\dot{m}$ mass flow rate, kg/s

N   plate number, -

NTU   number of transfer units, -

N_u Nusselt number, -

n   node number, -

P   perimeter, m

P_r Prandtl number, -

R_e Reynolds number, -

T   temperature, °C

t   time, s

t^* non-dimensional time, -

U   overall heat transfer coefficient, $kW/m^2/K$

u   specific internal energy, kJ/kg

$\bar{u}$ non-dimensional heat transfer coefficient, -

v   velocity, m/s

W   width, m

x   axial position, s

μ dynamic viscosity, Pa·s

ρ density, kg/m^3

τ non-dimensional time, -

χ liquid mass fraction, -

Subscripts and superscripts

f   fluid

i   node index

inl   inlet

l   liquid

m   melting

out   outlet

ref   reference

s   solid

′   new time step

Acronyms

GHG   greenhouse gas emissions

HTF   heat transfer fluid

IMO   International Maritime Organisation

LHTES   latent heat thermal energy storage

LNG   liquefied natural gas

PCM   phase change material

TES   thermal energy storage

WHR   waste heat recovery

References

[1] Singh D.V., Pedersen E., A review of waste heat recovery technologies for maritime applications. Energy Conversion and Management, 2016; 111: 315–28; doi.org:10.1016/j.enconman.2015.12.073.

[2] MAN Diesel & Turbo, Waste Heat Recovery System (WHRS) for Reduction of Fuel Consumption, Emissions and EEDI, 2014.

[3] United Nations, Developments in international seaborne trade, 2017; doi.org:10.18356/e9e3b605-en.

[4] Maritime Organisation International, Cutting GHG emissions from shipping – 10 years of mandatory rules, 2021; https://www.imo.org/en/MediaCentre/PressBriefings/pages/DecadeOfGHGAction.aspx [accessed 05.03.2023].

[5] Mallouppas G., Yfantis E.A., Decarbonization in Shipping industry: A review of research, technology development, and innovation proposals, Journal of Marine Science and Engineering, 2021; 9; doi.org:10.3390/jmse9040415.

[6] Morrison D.J., Performance of solar heating systems utilizing phase change energy storage, University of Wisconsin-Madison, 1976.

[7] Morrison D.J., Abdel-Khalik S.I., Effects of phase-change energy storage on the performance of air-based and liquid-based solar heating systems, Solar Energy, 1978; 20(1), 57–67; doi:10.1016/0038-092X(78)90141-X.

[8] Garg H.P., Mullick S.C., Bhargava, A.K., Solar Thermal Energy Storage. Springer Dordrecht, The Netherlands, 1985; doi:10.1007/978-94-009-5301-7.

[9] Majumdar P., Saidbakhsh A., A heat transfer model for phase change thermal energy storage, Heat Recovery Systems and CHP, 1990; 10(5–6); 457–468; doi: 10.1016/0890-4332(90)90196-Q.

[10] Duffie J.A., Beckman W.A., Solar Engineering of Thermal Processes (Fourth Edition), Wiley, 2013.

[11] Esteves L., Magalhães A., Ferreira V., Pinho C., Test of Two Phase Change Materials for Thermal Energy Storage: Determination of the Global Heat Transfer Coefficient, ChemEngineering, 2018; 2(1); 10; doi:10.3390/chemengineering2010010.

[12] Xu H., Yin Sze J., Romagnoli A., Py X., Selection of Phase Change Material for Thermal Energy Storage in Solar Air Conditioning Systems, Energy Procedia, 2017; 105; 4281–4288; doi: 10.1016/j.egypro.2017.03.898.